

PT phase transition and non-Hermitian skin effect in vacancy-induced subbands of the Haldane model with gain and loss

Cui-Xian Guo(郭翠仙), Xiao-Ming Zhao(赵小明), and Su-Peng Kou(寇谡鹏)
Citation: Chin. Phys. B, 2026, 35 (**4**): 047103. DOI: 10.1088/1674-1056/ae44f4
http://cpb.iphy.ac.cn; http://iopscience.iop.org/cpb

What follows is a list of articles you may be interested in

Gate leakage mechanisms in Al_2O_3/SiN/AlN/GaN MIS-HEMTs on Si substrates

Hui-Lin Li(李惠琳), Jie-Jie Zhu(祝杰杰), Ling-Jie Qin(秦灵洁), Si-Mei Huang(黄思美), Shi-Yang Li(李诗洋), Bo-Xuan Gao(高渤轩), Qing Zhu(朱青), and Xiao-Hua Ma(马晓华)
Chin. Phys. B, 2025, 34 (**4**): 047103. DOI: 10.1088/1674-1056/adb26d

Effects of vacancy and external electric field on the electronic properties of the $MoSi_2N_4$/graphene heterostructure

Qian Liang(梁前), Xiangyan Luo(罗祥燕), Guolin Qian(钱国林), Yuanfan Wang(王远帆), Yongchao Liang(梁永超), and Quan Xie(谢泉)
Chin. Phys. B, 2024, 33 (**3**): 037101. DOI: 10.1088/1674-1056/acef04

Saturation thickness of stacked SiO_2 in atomic-layer-deposited Al_2O_3 gate on 4H-SiC

Zewei Shao(邵泽伟), Hongyi Xu(徐弘毅), Hengyu Wang(王珩宇), Na Ren(任娜), and Kuang Sheng(盛况)
Chin. Phys. B, 2023, 32 (**8**): 087106. DOI: 10.1088/1674-1056/acd5c3

Helicity-dependent photoconductance of the edge states in the topological insulator Bi_2Te_3

Yuchao Zhou(周宇超), Jinling Yu(俞金玲), Yonghai Chen(陈涌海), Yunfeng Lai(赖云锋), and Shuying Cheng(程树英)
Chin. Phys. B, 2023, 32 (**8**): 087102. DOI: 10.1088/1674-1056/acc3fb

Non-Hermitian Kitaev chain with complex periodic and quasiperiodic potentials

Xiang-Ping Jiang(蒋相平), Yi Qiao(乔艺), and Junpeng Cao(曹俊鹏)
Chin. Phys. B, 2021, 30 (**7**): 077101. DOI: 10.1088/1674-1056/abfa08

$\mathcal{PT}$ phase transition and non-Hermitian skin effect in vacancy-induced subbands of the Haldane model with gain and loss

Cui-Xian Guo(郭翠仙)[1,2], Xiao-Ming Zhao(赵小明)[3,4], and Su-Peng Kou(寇谡鹏)[5,4,†]

[1] *Beijing Key Laboratory of Optical Detection Technology for Oil and Gas, China University of Petroleum-Beijing, Beijing* 102249, *China*
[2] *Basic Research Center for Energy Interdisciplinary, College of Science, China University of Petroleum-Beijing, Beijing* 102249, *China*
[3] *Department of Physics and Institute of Theoretical Physics, University of Science and Technology Beijing, Beijing* 100083, *China*
[4] *Key Laboratory of Multiscale Spin Physics (Ministry of Education), Beijing Normal University, Beijing* 100875, *China*
[5] *Center for Advanced Quantum Studies, School of Physics and Astronomy, Beijing Normal University, Beijing* 100875, *China*

(Received 13 November 2025; revised manuscript received 11 February 2026; accepted manuscript online 12 February 2026)

Defects can profoundly alter the properties of quantum materials, inducing emergent phenomena beyond the scope of their parent counterparts. Here, we construct effective models to investigate the properties of vacancy-induced subbands in the Haldane model with gain and loss, revealing that their behaviors are critically dependent on the spatial configuration of the vacancy array. Specifically, a sequence of parity–time ($\mathcal{PT}$) phase transitions occurs for the one-dimensional vacancy array across different sublattices, whereas the non-Hermitian skin effect (NHSE) — with its nontrivial spectral winding — manifests in a chain confined to a single sublattice. Notably, the NHSE arises in this subband even though the parent system lacks it. Our results demonstrate that vacancy defect engineering serves as a powerful approach to generate subsystems whose properties are decoupled from the parent Hamiltonian.

Keywords: non-Hermitian physics, defect, parity-time symmetry, non-Hermitian skin effect

PACS: 71.55.–i, 03.65.Yz, 11.30.Er, 73.20.–r

DOI: 10.1088/1674-1056/ae44f4 **CSTR:** 32038.14.CPB.ae44f4

1. Introduction

The past decade has witnessed a surge of interest in non-Hermitian physics,[1–6] extending its reach across optics,[7–13] acoustics,[14–17] photonic quantum walks[18,19] and single-spin systems.[20] This expansion has been driven by the discovery of novel phenomena without Hermitian counterparts. Two of the most remarkable are the parity–time ($\mathcal{PT}$) phase transition[14–22] and the non-Hermitian skin effect (NHSE).[28–40] The former describes a symmetry-breaking transition, marked by the spectrum becoming complex and the appearance of exceptional points (EPs) signaling the transition and the simultaneous coalescence of both eigenvalues and eigenstates. The NHSE manifests as the exponential boundary localization of an extensive number of eigenstates and is rooted in the nontrivial spectral winding of complex energy bands, which fundamentally reshapes the bulk–boundary correspondence in topological systems. These novel effects have subsequently spurred the development of innovative applications, such as unidirectional transport,[23,24] single-mode lasers[25,26] and optical funnels.[27]

Concurrently, defect engineering has long been established as a powerful tool for manipulating the properties of quantum materials.[41,42] In Hermitian settings, from dopants in semiconductors[43] to vacancies in graphene[44] and magnetic impurities in topological insulators,[45] defects can induce bound states, alter electronic structure and even generate entirely new phases of matter. The role of defects in non-Hermitian systems, however, presents a frontier rich with potential. A fundamental question persists: can a designed vacancy defect lattice in a non-Hermitian system yield a subsystem with emergent properties decoupled from, or absent in, the parent system?

In this work, we address this question by theoretically investigating vacancy-induced subbands in a non-Hermitian Haldane model under the periodic boundary condition (PBC). We construct effective models to elucidate the properties of these defect-engineered one-dimensional chains. Our key finding is that their behavior is critically governed by the spatial configuration of the vacancy array. We demonstrate that a chain of vacancies spanning different sublattices undergoes a sequence of $\mathcal{PT}$ phase transitions, whereas a chain confined to a single sublattice exhibits the NHSE, characterized by its nontrivial spectral winding. Strikingly, this NHSE emerges in the vacancy subband even when it is entirely absent in the parent system.

2. Model and single vacancy state

We investigate the non-Hermitian Haldane model[46] in the presence of vacancy defects. The total Hamiltonian is

†Corresponding author. E-mail: spkou@bnu.edu.cn

© 2026 Chinese Physical Society and IOP Publishing Ltd. All rights, including for text and data mining, AI training, and similar technologies, are reserved.

given by

$$\hat{H} = \hat{H}_0 + \hat{H}_{\rm v}, \tag{1}$$

where $\hat{H}_0$ represents the pristine non-Hermitian Haldane model on a honeycomb lattice with staggered imaginary on-site potentials, defined as

$$\begin{aligned}\hat{H}_0 \;=\; & -t\sum_{\langle i,j\rangle}(\hat{c}_i^{\dagger}\hat{c}_j + \text{h.c.}) - t'\sum_{\langle\langle i,j\rangle\rangle} \mathrm{e}^{\mathrm{i}\phi_{ij}}\hat{c}_i^{\dagger}\hat{c}_j \\ & + \sum_{i\in A}\mathrm{i}\gamma\hat{c}_i^{\dagger}\hat{c}_i - \sum_{i\in B}\mathrm{i}\gamma\hat{c}_i^{\dagger}\hat{c}_i,\end{aligned} \tag{2}$$

and $\hat{H}_{\rm v}$ is introduced to cancel the couplings and potentials at the vacancy sites

$$\begin{aligned}\hat{H}_{\rm v} \;=\; & t\sum_{\langle i\in\mathcal{V},j\rangle}(\hat{c}_i^{\dagger}\hat{c}_j + \text{h.c.}) + t'\sum_{\langle\langle i\in\mathcal{V},j\rangle\rangle} \mathrm{e}^{\mathrm{i}\phi_{ij}}\hat{c}_i^{\dagger}\hat{c}_j \\ & - \sum_{i\in\{A\cap\mathcal{V}\}}\mathrm{i}\gamma\hat{c}_i^{\dagger}\hat{c}_i + \sum_{i\in\{B\cap\mathcal{V}\}}\mathrm{i}\gamma\hat{c}_i^{\dagger}\hat{c}_i.\end{aligned} \tag{3}$$

Here t and t' denote the nearest-neighbor and next-nearest-neighbor hopping strengths, respectively. The phase factor is defined as $\phi_{ij} = \pm\pi/2$ for clockwise (counterclockwise) next-nearest-neighbor hopping. The gain and loss are implemented via on-site potentials $\mathrm{i}\gamma$ on sublattice A and $-\mathrm{i}\gamma$ on sublattice B, with γ quantifying the non-Hermitian strength. The set $\mathcal{V}$ denotes the indices of the vacancy defects.

Considering $\hat{H}_0$ under PBC as the parent system, the corresponding Bloch Hamiltonian is given by $\hat{H}(\boldsymbol{k}) = \sum_{\boldsymbol{k}}(\hat{a}_{\boldsymbol{k}}^{\dagger}, \hat{b}_{\boldsymbol{k}}^{\dagger})\mathcal{H}(\boldsymbol{k})(\hat{a}_{\boldsymbol{k}}, \hat{b}_{\boldsymbol{k}})^{\rm T}$, where

$$\mathcal{H}(\boldsymbol{k}) = \begin{pmatrix} \xi'_{\boldsymbol{k}} + \mathrm{i}\gamma & -\xi_{\boldsymbol{k}} \\ -\xi_{\boldsymbol{k}}^{*} & -\xi'_{\boldsymbol{k}} - \mathrm{i}\gamma \end{pmatrix}, \tag{4}$$

with

$$\xi_{\boldsymbol{k}} = t\sum_{i=1}^{3}\mathrm{e}^{\mathrm{i}\boldsymbol{k}\cdot\boldsymbol{a}_i}, \quad \xi'_{\boldsymbol{k}} = 2t'\sum_{i=1}^{3}\sin(\boldsymbol{k}\cdot\boldsymbol{b}_i). \tag{5}$$

The lattice vectors are defined as $\boldsymbol{a}_1 = a_0(0,1)$, $\boldsymbol{a}_2 = a_0\left(\frac{\sqrt{3}}{2}, -\frac{1}{2}\right)$, $\boldsymbol{a}_3 = a_0\left(-\frac{\sqrt{3}}{2}, -\frac{1}{2}\right)$, and $\boldsymbol{b}_1 = \boldsymbol{a}_2 - \boldsymbol{a}_3$, $\boldsymbol{b}_2 = \boldsymbol{a}_3 - \boldsymbol{a}_1$, $\boldsymbol{b}_3 = \boldsymbol{a}_1 - \boldsymbol{a}_2$ with $a_0 = 1$. The energy spectrum of the parent Hamiltonian reads

$$E_{\pm}(\boldsymbol{k}) = \pm\sqrt{|\xi_k|^2 + (\xi'_k + \mathrm{i}\gamma)^2}. \tag{6}$$

The eigenstates of this parent model are extended Bloch states, and no skin effect is present.

By adding $\hat{H}_{\rm v}$, we effectively create the vacancy defects. Therefore, our primary focus is to investigate the properties of the defect states induced by these vacancies in $\hat{H}$.

A single vacancy is created by removing a site i_0, as shown in Fig. 1(a), which eliminates both its on-site potential and all associated hopping terms. This defect gives rise to a bound state localized near the vacancy site (Fig. 1(b)), with the corresponding energy lying within the bulk band gap (Fig. 1(c)). Specifically, the defect state exhibits a purely imaginary energy: positive for a vacancy on sublattice B and negative for one on sublattice A (Fig. 1(d)).

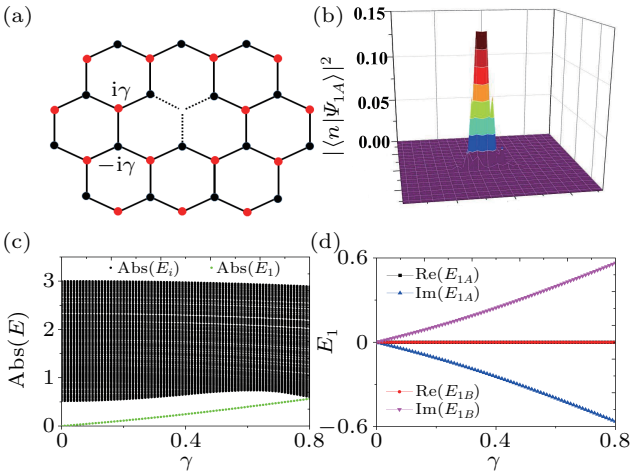


Fig. 1. (a) Schematic of the non-Hermitian Haldane model with a vacancy defect. (b) Spatial profile of a single A-sublattice defect state with $\gamma = 0.05$. (c) Energy spectra versus γ: bulk bands (black) and defect state energy (green). (d) Real and imaginary parts of the defect state energy as a function of γ. Common parameters: 36×36 lattice, $t = 1$ and $t' = 0.1$.

3. $\mathcal{PT}$-phase transition in subbands from vacancies on different sublattices

3.1. Effective model for two vacancies

We now examine the system described by Hamiltonian $\hat{H}(j_1, j_2)$ containing two vacancies located at sites j_1 and j_2 on different sublattices (A and B), separated by a distance L along the zigzag direction (Fig. 2(a)). The coupling between the corresponding defect states leads to inter-state tunneling. As shown in Figs. 2(b) and 2(c), our numerical results indicate that the eigenvalues of the two defect states undergo a $\mathcal{PT}$-phase transition as γ increases, accompanied by distinct changes in the eigenstates.

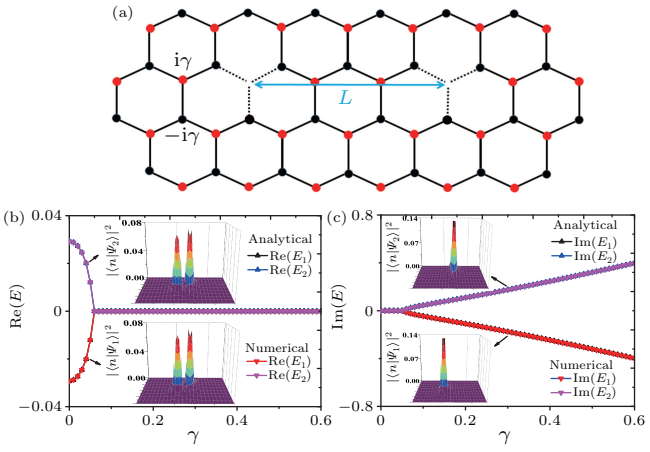


Fig. 2. (a) Two vacancies on different sublattices of the non-Hermitian Haldane model. (b) and (c) Real and imaginary parts of the two defect state energies versus γ. Insets: spatial profiles in the $\mathcal{PT}$-unbroken phase and $\mathcal{PT}$-broken phase. Parameters: 10×80 lattice, $t = 1$, $t' = 0.1$ and $L/|\boldsymbol{b}_1| = 3.5$.

To model this tunneling, we construct an effective Hamiltonian $\hat{H}_{\rm eff}$ within the biorthogonal subspace spanned by the single-vacancy eigenstates. Let $|V_i^{\rm R}\rangle$ and $\langle V_i^{\rm L}|$ denote the right and left eigenstates of the Hamiltonian $\hat{H}(j_i)$ containing a single vacancy at site j_i, satisfying $\hat{H}(j_i)|V_i^{\rm R}\rangle = E|V_i^{\rm R}\rangle$ and $\langle V_i^{\rm L}|\hat{H}(j_i) = \langle V_i^{\rm L}|E$. Assuming these states form a biorthogonal basis such that $\langle V_i^{\rm L}|V_j^{\rm R}\rangle = \delta_{ij}$, the effective Hamiltonian can then be obtained by projecting the full Hamiltonian $\hat{H}(j_1, j_2)$ onto this basis as $\hat{H}_{\rm eff} = (|V_1^{\rm R}\rangle, |V_2^{\rm R}\rangle)\mathcal{H}_{\rm eff}(\langle V_1^{\rm L}|, \langle V_2^{\rm L}|)^{\rm T}$, where

$$\mathcal{H}_{\rm eff} = \begin{pmatrix} h_{11} & h_{12} \\ h_{21} & h_{22} \end{pmatrix}, \tag{7}$$

with the matrix elements $h_{ij} = \langle V_i^{\rm L}|\hat{H}(j_1, j_2)|V_j^{\rm R}\rangle$.

Using the explicit forms of $|V_i^{\rm R}\rangle$ and $\langle V_i^{\rm L}|$, we derive the effective Hamiltonian

$$\mathcal{H}_{\rm eff} = h_x\sigma_x + {\rm i}h_y\sigma_y - {\rm i}h_z\sigma_z. \tag{8}$$

Here $\sigma_{x,y,z}$ are Pauli matrices and $h_x, h_y, h_z \in \mathbb{R}$. Figure 3(a) illustrates the evolution of h_x, h_y and h_z as a function of γ for $L/|\boldsymbol{b}_1| = 3.5$. Since $h_y \approx 0$, we neglect this term, allowing the effective Hamiltonian to be approximated as

$$\mathcal{H}_{\rm eff} \approx h_x\sigma_x - {\rm i}h_z\sigma_z, \tag{9}$$

yielding the eigenvalues

$$E_{1,2} = \pm\sqrt{h_x^2 - h_z^2}. \tag{10}$$

This effective Hamiltonian possesses $\mathcal{PT}$ symmetry: $[\hat{H}_{\rm eff}, \mathcal{PT}] = 0$, where $\mathcal{P} = \sigma_x$ and $\mathcal{T}$ denotes complex conjugation. The system resides in the $\mathcal{PT}$-unbroken phase when $|h_x| > |h_z|$, characterized by two real eigenvalues E_1 and E_2. Conversely, when $|h_z| > |h_x|$, the system enters the $\mathcal{PT}$-broken phase, and the eigenvalues become purely imaginary. The EP emerges at $|h_z| = |h_x|$ (i.e., at $\gamma = \gamma_0$), marked by the simultaneous coalescence of eigenvalues and eigenstates.

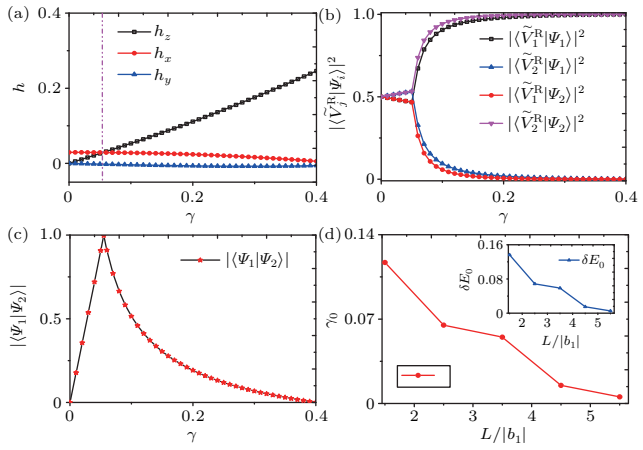


Fig. 3. (a) Matrix elements of the effective model in Eq. (9) versus γ. (b) Spatial distribution of the defect states characterized by their projection onto the normalized single-vacancy basis vectors versus γ. Parameters for panel (a)–(c): $L/|\boldsymbol{b}_1| = 3.5$. (d) Phase transition point γ_0 versus L. Inset: the initial energy level splitting δE_0 versus L. Common parameters: 10×80 lattice, $t = 1, t' = 0.1$.

To quantify the spatial distribution of the defect states over the two vacancy sites, we calculate the projection of the defect states $|\Psi_i\rangle$ onto the normalized right basis vectors $|\widetilde{V}_j^{\rm R}\rangle$, defined as $|\widetilde{V}_j^{\rm R}\rangle = |V_j^{\rm R}\rangle/\sqrt{\langle V_j^{\rm R}|V_j^{\rm R}\rangle}$. Note that the defect states $|\Psi_i\rangle$ are self-normalized (i.e., $\langle\Psi_i|\Psi_i\rangle = 1$) by default. This normalization ensures that the projection reflects the physical weight of the defect states on each vacancy site. Figure 3(b) illustrates the squared overlap $|\langle\widetilde{V}_j^{\rm R}|\Psi_i\rangle|^2$ as a function of γ. In the $\mathcal{PT}$-unbroken phase, the defect states are distributed nearly uniformly across the two vacancy sites (with minor deviations from perfect uniformity attributed to the h_y term). In contrast, in the $\mathcal{PT}$-broken regime, these states rapidly localize onto separate vacancies as γ increases. Figure 3(c) plots the similarity $\langle\Psi_1|\Psi_2\rangle$ between the two defect states. At the EP, the similarity reaches unity, indicating state coalescence, as predicted by the effective model. The analytical eigenenergies from the effective model agree closely with numerical results (Figs. 2(b) and 2(c)), validating our approach. While the distance between the two vacancies is fixed $L/|\boldsymbol{b}_1| = 3.5$ in Figs. 3(a)–3(c), figure 3(d) subsequently demonstrates the influence of the vacancy separation L on both the transition point γ_0 and the initial energy level splitting at $\gamma = 0$ (inset). Figure 3(d) illustrates the dependence of the transition point γ_0 on the vacancy separation L, while the inset displays the initial energy level splitting $\delta E_0 = |E_1(\gamma = 0) - E_2(\gamma = 0)|$ between the two defect states, which represents the intrinsic tunneling strength in the Hermitian limit. The results indicate that as the vacancy distance increases, the tunnel coupling between the two defect states weakens at $\gamma = 0$, which consequently leads to an earlier onset of the $\mathcal{PT}$-broken phase with increasing γ.

3.2. $\mathcal{PT}$-phase transition for a one-dimensional vacancy array on different sublattices

Here, we extend our investigation to a one-dimensional (1D) array of N alternating A–B vacancies located at sites $j_1 \cdots j_N$ along the zigzag direction (i.e., the x-direction), with adjacent spacing L. Generalizing the two-vacancy case, we construct an effective non-Hermitian tight-binding Hamiltonian to describe this subsystem

$$\begin{aligned}\hat{H}_{\rm eff} = & -{\rm i}h_z(\gamma)\sum_{j\in A}\hat{c}_j^\dagger\hat{c}_j + {\rm i}h_z(\gamma)\sum_{j\in B}\hat{c}_j^\dagger\hat{c}_j \\ & + h_x(\gamma)\sum_j(\hat{c}_j^\dagger\hat{c}_{j+1} + \hat{c}_{j+1}^\dagger\hat{c}_j),\end{aligned} \tag{11}$$

where $\hat{c}_j^\dagger$ and $\hat{c}_j$ ($j = j_1 \cdots j_N$) represent the particle creation and annihilation operators at the vacancy site j. Here $h_x(\gamma)$ is the coupling between the nearest-neighbor sites, and $\pm{\rm i}h_z(\gamma)$ are the on-site potentials on B or A sublattices, respectively. The γ-dependence of $h_x(\gamma)$ and $h_z(\gamma)$ follows from the two-defect analysis.

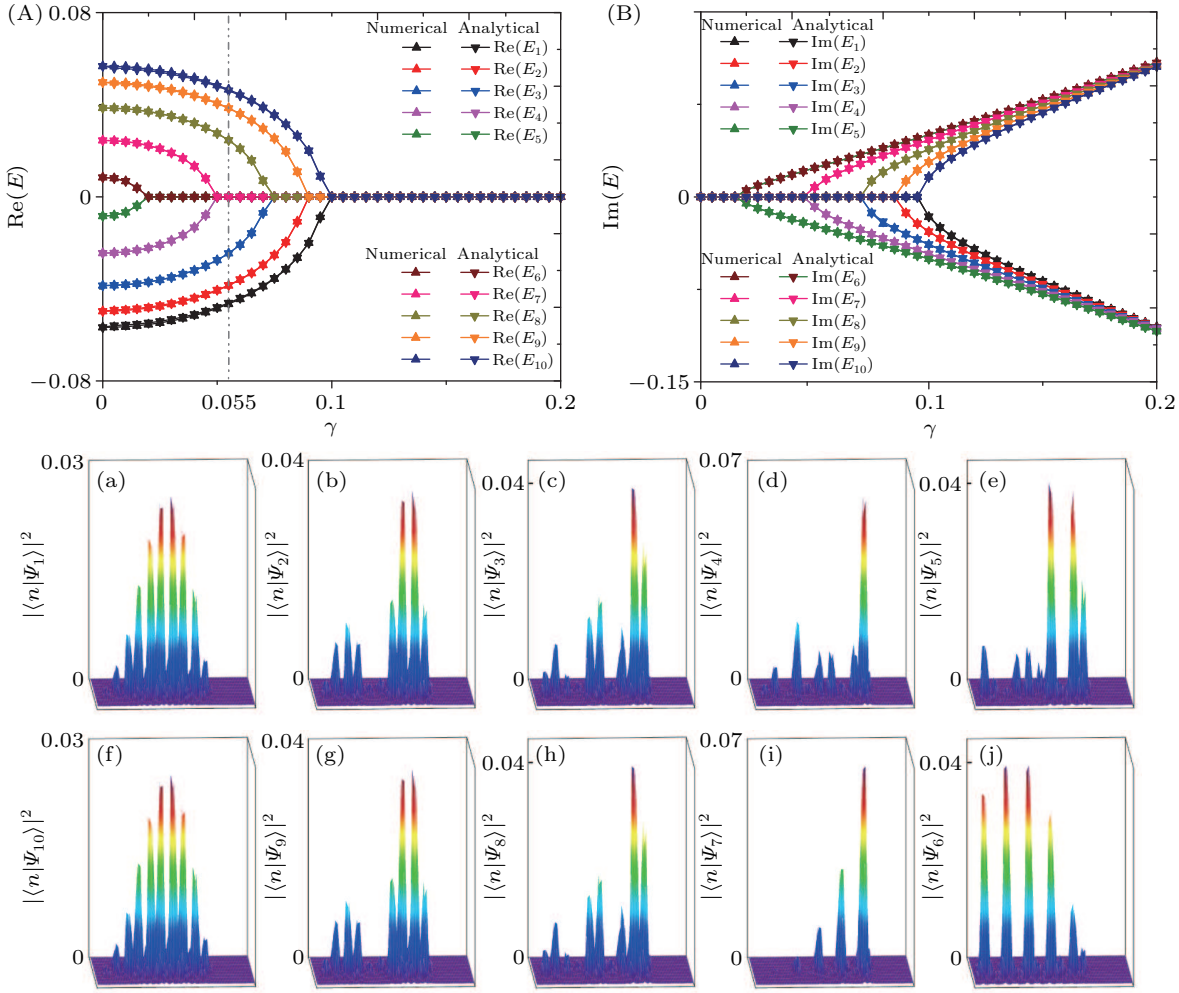


Fig. 4. (A) and (B) Real and imaginary parts of the defect state energies versus γ for the non-Hermitian Haldane model with ten vacancies on different sublattices. (a)–(j) Spatial profiles of the ten defect states at $\gamma = 0.055$. Common parameters: 10×100 lattice, $t = 1$, $t' = 0.1$, $L/|\boldsymbol{b}_1| = 3.5$.

For a periodic defect array, we apply the Fourier transform $\hat{c}_{j\in A} = \frac{1}{\sqrt{N}} \sum_{k_x} \mathrm{e}^{\mathrm{i}k_x \boldsymbol{R}_j} \hat{a}_{k_x}$, $\hat{c}_{j\in B} = \frac{1}{\sqrt{N}} \sum_{k_x} \mathrm{e}^{-\mathrm{i}k_x \boldsymbol{R}_j} \hat{b}_{k_x}$, yielding the momentum-space effective Hamiltonian $\hat{H}_{\mathrm{eff}}(k_x) = \sum_{k_x} (\hat{a}^\dagger_{k_x}, \hat{b}^\dagger_{k_x}) \mathcal{H}_{\mathrm{eff}}(k_x) (\hat{a}_{k_x}, \hat{b}_{k_x})^{\mathrm{T}}$ with

$$\mathcal{H}_{\mathrm{eff}}(k_x) = h_x(\gamma)\cos(k_x)\sigma_x - \mathrm{i}h_z(\gamma)\sigma_z.$$

Diagonalizing $\mathcal{H}_{\mathrm{eff}}(k_x)$ gives the spectrum

$$E_{\pm k_x} = \pm\sqrt{[h_x(\gamma)\cos(k_x)]^2 - [h_z(\gamma)]^2}.$$

The effective Hamiltonian $\hat{H}_{\mathrm{eff}}(k_x)$ possesses $\mathcal{PT}$ symmetry $[\hat{H}_{\mathrm{eff}}(k_x), \mathcal{PT}] = 0$, where $\mathcal{P} = \sigma_x$ and $\mathcal{T}$ performs complex conjugation.

For a fixed momentum k_x, the system is in the $\mathcal{PT}$-unbroken phase when $|h_z(\gamma)| < |h_x(\gamma)\cos(k_x)|$, yielding real eigenvalues $E_\pm(k_x)$. When $|h_z(\gamma)| > |h_x(\gamma)\cos(k_x)|$, the eigenvalues become purely imaginary, corresponding to the $\mathcal{PT}$-broken phase. The EP occurs at $|h_z(\gamma)| = |h_x(\gamma)\cos(k_x)|$. The $\mathcal{PT}$ phase transition depends on k_x, and symmetry breaking occurs gradually in pairs of $\mathcal{PT}$-symmetric dimers as γ varies.

Figures 4(A) and 4(B) present the real and imaginary parts of the analytical and numerical energies for the ten defect states as a function of γ. The defect states form $\mathcal{PT}$-symmetric pairs that sequentially transition into the $\mathcal{PT}$-broken phase as γ increases. The paired states in the $\mathcal{PT}$-unbroken phase share identical spatial distributions spanning multiple defect sites [Figs. 4(a)–4(c) and 4(f)–4(h)], whereas the distributions of the remaining $\mathcal{PT}$-broken pairs become distinct [Figs. 4(d), 4(e) and 4(i), 4(j)]. These results align with the predictions of our effective model. Furthermore, we observe that many states exhibit a spatial asymmetry (with higher probability weights on the right-side defects). This likely originates from the h_y term — which is neglected in our effective model — analogous to the mechanism discussed in the two-defect case.

4. NHSE in subbands from vacancies on the same sublattices

4.1. Effective model for two vacancies

We next analyze two vacancies on the same sublattices (e.g., A-sublattice), separated by a distance L along the zigzag direction (Fig. 5(a)). The tunneling between the two defect states differs from that in the different-sublattice case. As shown in Figs. 5(b) and 5(c), the eigenvalues of the two de-

fect states undergo a spectral transition from complex to purely imaginary as γ increases.

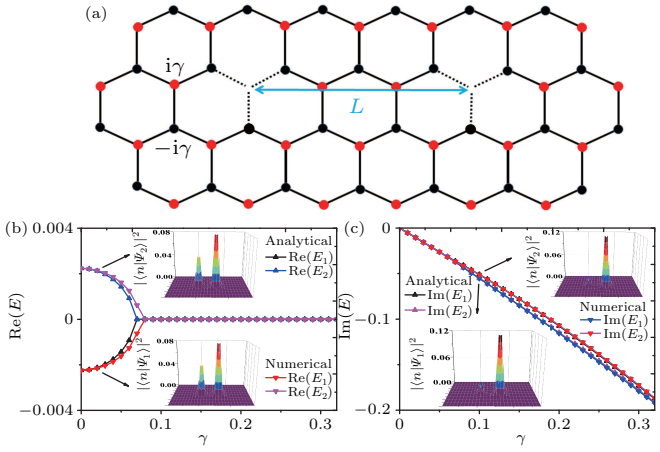


Fig. 5. (a) Schematic of two vacancies on the same sublattice (*A*-sublattice) of the non-Hermitian Haldane model. (b) and (c) Real and imaginary parts of the two defect states versus γ. Insets: spatial profiles of the two defect states before and after the spectral transition from complex to purely imaginary. Parameters: 10×80 lattice, $t=1$, $t'=0.1$ and $L/|\boldsymbol{b}_1|=6$.

Within the framework established in the preceding section, we model the tunneling via the effective Hamiltonian

$$\hat{H}_{\rm eff}=\mathrm{i}h_x\sigma_x+h_y\sigma_y+\mathrm{i}h_0\sigma_0, \tag{12}$$

with eigenvalues

$$E_{1,2}=\pm\sqrt{h_y^2-h_x^2}+\mathrm{i}h_0. \tag{13}$$

Here $\sigma_{x,y}$ are Pauli matrices, σ_0 is the 2×2 identity matrix and h_x, h_y, and h_0 are real γ-dependent parameters plotted in Fig. 6(a). For $\gamma<0.15$, h_y remains nearly constant while h_x increases approximately linearly with γ. The effective Hamiltonian is non-Hermitian and respects sublattice symmetry: $\sigma_z\hat{H}_{\rm eff}\sigma_z=-\hat{H}_{\rm eff}$.

At the critical value γ_0, where $h_x=h_y$, the effective Hamiltonian reduces to $\hat{H}_{\rm eff}=2\mathrm{i}h_x\sigma_-+\mathrm{i}h_0\sigma_0$ with $\sigma_-=\frac{1}{2}(\sigma_x-\mathrm{i}\sigma_y)$, signaling an EP. Here, both eigenvalues and eigenvectors coalesce: $E_1=E_2=\mathrm{i}h_0$ and $|\psi_1\rangle=|\psi_2\rangle=(0,1)^{\rm T}$. As γ increases and surpasses the critical value γ_0, the energy spectrum undergoes a transition from complex to purely imaginary, with the EP at $\gamma=\gamma_0$ marking this critical point of transition.

Figure 6(b) illustrates the projection of the two defect states onto the selected basis, and figure 6(c) displays their similarity $|\langle\psi_1|\psi_2\rangle|$. For $\gamma\neq 0$, both defect states tend to be more localized at the right vacancy defect. As the system approaches the EP, the disparity in distribution between the two vacancies becomes more pronounced. At the EP (i.e., $\gamma=\gamma_0$), both defect states become completely localized at the right vacancy defect, with a similarity of 1, consistent with the predictions of our effective model. The analytical eigenenergies from the effective model agree closely with numerical results (Figs. 5(b) and 5(c)). With the distance between vacancies fixed at $L/|\boldsymbol{b}_1|=6$ in Figs. 6(a)–6(c), figure 6(d) examines the dependence of both the transition point γ_0 and the initial energy level splitting (inset) on the vacancy separation L. It is shown that the tunneling effect at $\gamma=0$ is suppressed by increasing L, and the occurrence of the EP for $\gamma\neq 0$ is explicitly shown to depend on L.

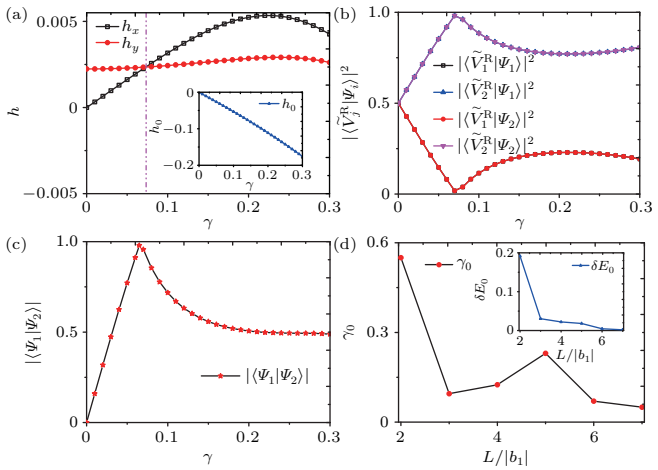


Fig. 6. (a) Matrix elements of the effective model in Eq. (12) versus γ. (b) Projection of the two defect states onto the selected basis vectors versus γ. (c) Similarity between the two defect states versus γ. Parameters for (a)–(c): $L/|\boldsymbol{b}_1|=6$. (d) Phase transition point γ_0 versus distance L. Inset: the initial energy level splitting δE_0 versus L. Common parameters: 10×80 lattice, $t=1$, $t'=0.1$.

4.2. NHSE for 1D vacancy array on the same sublattice

Having established the formation of a non-Hermitian dimer from two vacancies on the same sublattice, we extend our analysis to a 1D array of N such vacancies located at sites $j_1\cdots j_N$, all residing on the same A-sublattice with period L along the zigzag direction (i.e., the x-direction). This subsystem can be described by the tight-binding Hamiltonian with nonreciprocal hopping:

$$\begin{aligned}\hat{H}_{\rm eff}\;=\;&\mathrm{i}h_0(\gamma)\sum_j\hat{c}_j^\dagger\hat{c}_j+\mathrm{i}[h_x(\gamma)-h_y(\gamma)]\sum_j(\hat{c}_j^\dagger\hat{c}_{j+1})\\&+\mathrm{i}[h_x(\gamma)+h_y(\gamma)]\sum_j(\hat{c}_{j+1}^\dagger\hat{c}_j),\end{aligned} \tag{14}$$

where $\hat{c}_j^\dagger$ and $\hat{c}_j$ $(j=j_1\cdots j_N)$ represent the particle creation and annihilation operators at the vacancy site j, $\mathrm{i}[h_x(\gamma)\pm h_y(\gamma)]$ is the nonreciprocal hopping amplitudes between nearest-neighbor sites and $\mathrm{i}h_0(\gamma)$ is the on-site potential. The parameters $h_x(\gamma)$, $h_z(\gamma)$ and $h_0(\gamma)$ evolve with γ, following the behavior established in the two-vacancy scenario.

For a periodic vacancy array, we apply the Fourier transform $\hat{c}_j=\frac{1}{\sqrt{N}}\sum_{k_x}\mathrm{e}^{\mathrm{i}k_x\boldsymbol{R}_j}\hat{a}_{k_x}$, yielding the momentum-space effective Hamiltonian $\hat{H}_{\rm eff}(k_x)=\sum_{k_x}\hat{a}_{k_x}^\dagger\mathcal{H}_{\rm eff}(k_x)\hat{a}_{k_x}$ with

$$\mathcal{H}_{\rm eff}(k_x)=2\mathrm{i}h_x(\gamma)\cos(k_x)+2h_y(\gamma)\sin(k_x)+\mathrm{i}h_0(\gamma) \tag{15}$$

and energy spectrum

$$E_{\rm eff}(k_x) = 2ih_x(\gamma)\cos(k_x) + 2h_y(\gamma)\sin(k_x) + ih_0(\gamma). \quad (16)$$

Figure 7(a) shows the complex energy spectrum for the non-Hermitian Haldane model with 20 A-sublattice vacancies, where the vacancies form a periodic lattice. The defect state energies lie within the bulk gap and form a closed loop in the complex plane (Fig. 7(b)), indicating nontrivial spectral topology. Figure 7(c) plots the γ-dependence of the effective Hamiltonian matrix elements following the two A-sublattice vacancies scenario.

Using the extracted values $h_x(0.05)$, $h_y(0.05)$ and $h_0(0.05)$ in Fig. 7(c), we compute $E_{\rm eff}$ from Eq. (16). The resulting closed energy loop in Fig. 7(d) matches the numerical results in Fig. 7(b), validating our effective model. The nonzero spectral winding around points such as d_1 or d_2 implies the presence of the NHSE for the vacancy array subsystem under open boundary condition.

To verify the NHSE in this 1D vacancy–defect subsystem, we construct eight vacancies on the A-sublattice with open boundaries embedded in the parent model. Figures 8(A) and 8(B) display the real and imaginary parts of the energies for eight defect states as a function of γ. Their spatial profiles at $\gamma = 0.05$ (Figs. 8(a)–8(h)) reveal that all eigenmodes are localized toward the left vacancy boundary, demonstrating that the subsystem exhibits the NHSE as predicted by our effective model. Strikingly, this pronounced skin localization emerges in the 1D A-sublattice vacancy array subsystem, even though the parent model itself lacks the NHSE.

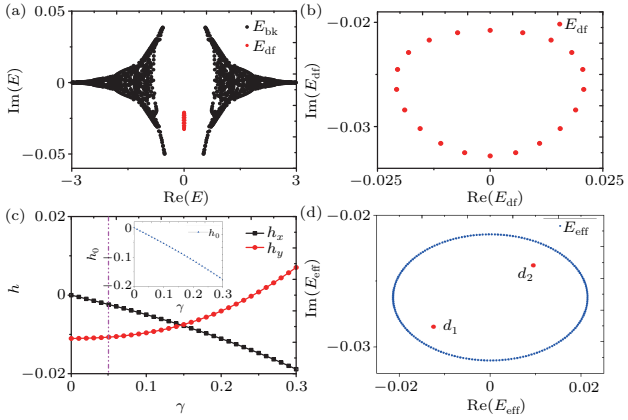


Fig. 7. (a) Complex energy spectrum for the non-Hermitian Haldane model with 20 A-sublattice vacancies, where the vacancies form a periodic lattice. (b) Complex energy spectrum of the defect lattice subsystem in panel (a). (c) Matrix elements of the effective Hamiltonian for two A-sublattice vacancies versus γ. (d) Complex energy spectrum $E_{\rm eff}$ from Eq. (16) for the 1D periodic defect array; d_1, d_2 are reference points. Parameters for panels (a), (b), (d): $\gamma = 0.05$. Common parameters: 10×160 lattice, $t = 1$, $t' = 0.1$, $L/|\boldsymbol{b}_1| = 4$.

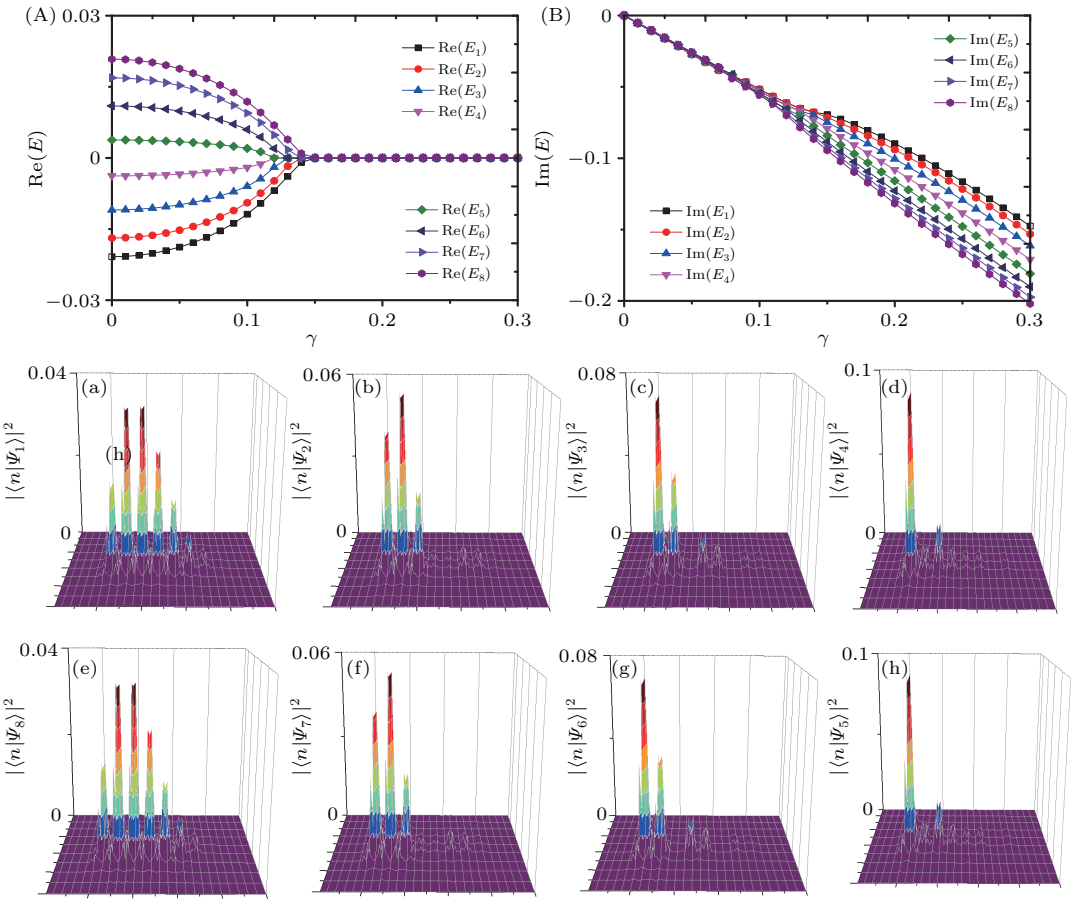


Fig. 8. (A) and (B) Real and imaginary parts of the defect state energies versus γ based on numerical results for the non-Hermitian Haldane model with eight A-sublattice vacancies, where the vacancy array forming a 1D open-boundary subsystem. (a)–(h) Spatial profiles of the eight defect states at $\gamma = 0.05$. Parameters: 10×100 lattice, $t = 1$, $t' = 0.1$, $L/|\boldsymbol{b}_1| = 4$.

5. Conclusion

In summary, we have systematically investigated the emergent phenomena in vacancy-induced subbands within a non-Hermitian Haldane model. By constructing effective models, we have demonstrated that the spatial configuration of the vacancy array dictates the fundamental character of the resulting subsystem. For a 1D chain of vacancies alternating between different sublattices, the subsystem exhibits a sequence of $\mathcal{PT}$ phase transitions, with eigenvalues transitioning from real to imaginary pairs. In stark contrast, a vacancy chain confined to a single sublattice gives rise to the NHSE, characterized by nontrivial spectral winding. The most profound implication of our work is the demonstration that vacancy defect engineering can create effective subsystems whose physical properties are entirely decoupled from those of the parent Hamiltonian. The emergence of the NHSE in a single-sublattice vacancy chain — despite its absence in the parent system — highlights the power of this approach.

Acknowledgments

Project supported by the National Natural Science Foundation of China (Grant No. 12405030), the National Key Research and Development Program of China (Grant No. 2023YFA1406704), the Open Fund of Key Laboratory of Multiscale Spin Physics (Ministry of Education) Beijing Normal University (Grant No. SPIN2024K01), Beijing National Laboratory for Condensed Matter Physics (Grant No. 2025BNLCMPKF023), the Science Foundation of China University of Petroleum, Beijing (Grant No. 2462024SZBH003), Young Elite Scientists Sponsorship Program of the Beijing High Innovation Plan (Grant No. 20250934), Guangdong Basic and Applied Basic Research Foundation (Grant No. 2023A1515110081), and Fundamental Research Funds for the Central Universities, China (Grant Nos. FRF-TP-22-098A1 and FRF-IDRY-24-28).

References

[1] Ashida Y, Gong Z and Ueda M 2020 *Adv. Phys.* **69** 249
[2] Bergholtz E J, Budich J C and Kunst F K 2021 *Rev. Mod. Phys.* **93** 015005
[3] Ding K, Fang C and Ma G 2022 *Nat. Rev. Phys.* **4** 745
[4] Moiseyev N 2011 *Non-Hermitian Quantum Mechanics* (New York: Cambridge University Press)
[5] Bender C M 2007 *Rep. Prog. Phys.* **70** 947
[6] Yang K, Li Z, König J L K, Rødland L, Stålhammar M and Bergholtz E J 2024 *Rep. Prog. Phys.* **87** 078002
[7] Guo A, Salamo G J, Duchesne D, Morandotti R, VolatierRavat M, Aimez V, Siviloglou G A and Christodoulides D N 2009 *Phys. Rev. Lett.* **103** 093902
[8] Rüter C E, Makris K G, El-Ganainy R, Christodoulides D N, Segev M and Kip D 2010 *Nat. Phys.* **6** 192
[9] Chong Y D, Ge L and Stone A D 2011 *Phys. Rev. Lett.* **106** 093902
[10] Regensburger A, Bersch C, Miri M A, Onishchukov G, Christodoulides D N and Peschel U 2012 *Nature* **488** 167
[11] Feng L, Xu Y L, Fegadolli W S, Lu M H, Oliveira J E B, Almeida V R, Chen Y F and Scherer A 2013 *Nat. Mater.* **12** 108
[12] Wimmer M, Miri M A, Christodoulides D N and Peschel U 2015 *Sci. Rep.* **5** 17760
[13] Weimann S, Kremer M, Plotnik Y, Lumer Y, Nolte S, Makris K G, Segev M, Rechtsman M C and Szameit A 2017 *Nat. Mater.* **16** 433
[14] Zhu X, Ramezani H, Shi C, Zhu J and Zhang X 2014 *Phys. Rev. X* **4** 031042
[15] Popa B I and Cummer S A 2014 *Nat. Commun.* **5** 3398
[16] Fleury R, Sounas D and Alu A 2015 *Nat. Commun.* **6** 5905
[17] Ding K, Ma G, Xiao M, Zhang Z Q and Chan C T 2016 *Phys. Rev. X* **6** 021007
[18] Xiao L, Deng T, Wang K, Wang Z, Yi W and Xue P 2021 *Phys. Rev. Lett.* **126** 230402
[19] Wang K, Xiao L, Budich J C, Yi W and Xue P 2021 *Phys. Rev. Lett.* **127** 026404
[20] Wu Y, Liu W, Geng J, Song X, Ye X, Duan C K, Rong X and Du J 2019 *Science* **364** 878
[21] Bender C M and Boettcher S 1998 *Phys. Rev. Lett.* **80** 5243
[22] Hang C, Huang G and Konotop V V 2013 *Phys. Rev. Lett.* **110** 083604
[23] Feng L, Xu Y L, Fegadolli W S, Lu M H, Oliveira J E B, Almeida V R, Chen Y F and A Scherer 2013 *Nat. Mater.* **12** 108
[24] Peng B, Özdemir Ş K, Lei F, Monifi F, Gianfreda M, Long G L, Fan S, Nori F, Bender C M and Yang L 2014 *Nat. Phys.* **10** 394
[25] Feng L, Wong Z J, Ma R M, Wang Y and Zhang X 2014 *Science* **346** 972
[26] Hodaei H, Miri M A, Heinrich M, Christodoulides D N and Khajavikhan M 2014 *Science* **346** 975
[27] Weidemann S, Kremer M, Helbig T, Hofmann T, Stegmaier A, Greiter M, Thomale R and Szameit A 2020 *Science* **368** 311
[28] Yao S and Wang Z 2018 *Phys. Rev. Lett.* **121** 086803
[29] Yokomizo K and Murakami S 2019 *Phys. Rev. Lett.* **123** 066404
[30] Kunst F K, Edvardsson E, Budich J C and Bergholtz E J 2018 *Phys. Rev. Lett.* **121** 026808
[31] Zhang K, Yang Z and Fang C 2020 *Phys. Rev. Lett.* **125** 126402
[32] Okuma N, Kawabata K, Shiozaki K and Sato M 2020 *Phys. Rev. Lett.* **124** 086801
[33] Yang Z, Zhang K, Fang C and Hu J 2020 *Phys. Rev. Lett.* **125** 226402
[34] Alvarez V M M, Vargas J E B and Torres L E F F 2018 *Phys. Rev. B* **97** 121401
[35] Borgnia D S, Kruchkov A J and Slager R J 2020 *Phys. Rev. Lett.* **124** 056802
[36] Guo C X, Liu C H, Zhao X M, Liu Y and Chen S 2021 *Phys. Rev. Lett.* **127** 116801
[37] Lee C H and Thomale R 2019 *Phys. Rev. B* **99** 201103
[38] Wang H Y, Song F and Wang Z 2024 *Phys. Rev. X* **14** 021011
[39] Hu H 2025 *Sci. Bull.* **70** 51
[40] Zhang K, Yang Z and Fang C 2022 *Nat. Commun.* **13** 2496
[41] Fu B, Jia Z, Mu W, Yin Y, Zhang J and Tao X 2019 *J. Semicond.* **40** 011804
[42] Klimov P V and Awschalom D D 2025 *Appl. Sci.* **15** 5606
[43] Pearton S J, Norton D P, Ip K, Heo Y W and Steiner T 2004 *J. Vac. Sci. Technol. B* **22** 932
[44] Ugeda M M, Brihuega I, Guinea F and Gómez-Rodríguez J M 2010 *Phys. Rev. Lett.* **104** 096804
[45] Schlenk T, Bair M, Wiebe J and Wiesendanger R 2012 *Phys. Rev. Lett.* **108** 066801
[46] Haldane F D M 1988 *Phys. Rev. Lett.* **61** 2015